

# Neutron DVCS Measurements with BONuS12 in CLAS12

M. Hattawy<sup>†‡</sup>, S. Bültmann, N. Dzubenski, S. Kuhn, D. Payette, J. Poudel

*Old Dominion University, Norfolk, VA 23529, USA*

R. Dupré, M. Ehrhart, M. Guidal, D. Marchand, C. Muñoz, S. Niccolai, E. Voutier  
*Institut de Physique Nucléaire, CNRS-IN2P3, Univ. Paris-Sud, Université Paris-Saclay,  
91406 Orsay Cedex, France*

N. Baltzell, F. X. Girod, S. Stepanyan

*Thomas Jefferson National Accelerator Facility, Newport News, VA 23606, USA*

N. Kalantarians

*Virginia Union University, 1500 N. Lombardy St., Richmond, VA 23220, USA*

## a CLAS Collaboration Proposal

---

<sup>‡</sup>Contact person

## Abstract

The three-dimensional picture of quarks and gluons in the nucleon is set to be revealed through deeply virtual Compton scattering (DVCS). With the absence of a free neutron target, the deuterium target represents the simplest nucleus to be used to probe the internal 3D partonic structure of the quasi-free neutron. We propose to measure the beam spin asymmetry (BSA) in incoherent neutron DVCS together with the approved BONuS12 experiment, using the same beam time and are asking for the electron beam to be highly polarized. The DVCS BSA on a (quasi-free) neutron will be measured in a wide range of kinematics by tagging the scattered electron and the real photon final state with the spectator proton. We will also measure BSA with all final state particles detected; the scattered electron, the real photon, the spectator proton, and the struck neutron. Both measurements of BSA of neutron DVCS, by tagging the recoil proton and in the fully exclusive final state, will help to understand the impact of the final state interactions (FSI) and Fermi motion on the incoherent neutron DVCS. The proposed measurements are highly complementary to the approved CLAS12 experiment E12-11-003, which will also measure the quasi-free neutron DVCS by detecting the scattered neutron.

# Contents

<b>Abstract</b>	<b>5</b>
<b>Introduction</b>	<b>7</b>
<b>1 Neutron Partonic Structure</b>	<b>9</b>
1.1 Physics motivations: Neutron GPDs . . . . .	9
1.2 DVCS Formalism and Observables . . . . .	9
1.3 Tagged neutron DVCS with BONuS12 . . . . .	13
1.4 Fully exclusive neutron DVCS with BONuS12 . . . . .	14
<b>2 Run conditions and Experimental setup</b>	<b>16</b>
2.1 Run Group F conditions . . . . .	16
2.2 The CLAS12 Spectrometer . . . . .	16
2.3 BONuS12 RTPC . . . . .	16
<b>3 Projections for the Proposed Measurements</b>	<b>20</b>
3.1 Monte-Carlo Simulation . . . . .	20
3.2 Projections . . . . .	21
3.2.1 Semi-exclusive selection . . . . .	21
3.2.2 Semi-exclusive selection . . . . .	21
<b>Summary</b>	<b>27</b>

# Introduction

Inclusive deep inelastic scattering (DIS) experiments have been instrumental in advancing our understanding of the QCD structure of nuclei and the effect of nuclear matter on the structure of hadrons. A great example is the observation by the European Muon Collaboration (EMC) of a deviation of the deep inelastic structure function of a nucleus from the sum of the structure functions of the free nucleons, the so-called EMC effect [1]. It became clear that even in a DIS process characterized by high locality of the probe-target interaction region, a different picture emerges from the nucleus other than a collection of quasi-free nucleons. On the theory side, despite decades of theoretical efforts [2–6] with increased sophistication, a unifying physical picture of the origin of the EMC effect is still a matter of intense debate. To reach the next level of our understanding of nuclear QCD and unravel the partonic structure of nuclei, experiments need to go beyond the inclusive measurements and focus on exclusive and semi-inclusive reactions.

Hard exclusive experiments such as Deeply Virtual Compton Scattering (DVCS) and Deeply Virtual Meson Production (DVMP) provide an important new probe that allows us to discern among the different interpretations of nuclear effects on the structure of embedded nucleons in the nuclear medium. By introducing a new framework to describe both the intrinsic motion of partons and their transverse spatial structure in nuclei [4–9], valuable information can be obtained from the measurement of the nuclear Generalized Parton Distributions (GPDs) representing the soft matrix elements for these processes. The GPDs correspond to the coherence between quantum states of different (or same) helicity, longitudinal momentum, and transverse position. In an impact parameter space, they can be interpreted as a distribution in the transverse plane of partons carrying a certain longitudinal momentum [10–12]. A crucial feature of GPDs is the access to the transverse position of partons which, combined with their longitudinal momentum, leads to the total angular momentum of partons [13]. This information is not accessible to inclusive DIS which measures probability amplitudes in the longitudinal plane.

A high luminosity facility such as Jefferson Lab offers a unique opportunity to map out the three-dimensional quark and gluon structure of nucleons and nuclei. While most of submitted proposals to JLab Program Advisory Committee (PAC) have focused on the studies of the 3D proton structure considered as one of the main motivations for the JLab 12 GeV upgrade, we

propose here to extend the measurements to quasi-free neutrons in deuterium with BONuS12 experiment.

# Chapter 1

## Neutron Partonic Structure

### 1.1 Physics motivations: Neutron GPDs

Electromagnetic probes have played a major role in advancing our knowledge about the structure of the nucleon. While lepton-nucleon elastic scattering measurements have taught us about the spatial charge and magnetization distributions [14, 15], deep-inelastic scattering experiments have uncovered the partonic structure of the nucleon and the longitudinal momentum distributions of the constituent partons, i.e., quarks and gluons [16]. With nuclear targets, deeply inelastic lepton scattering measurements have revealed that the distribution of quarks in a nucleus is not a simple convolution of their distributions within nucleons, an observation known as the “EMC effect” [17] (for reviews on the topic, see [18–21]).

A wealth of information on the structure of hadrons lies in the correlations between the momentum and spatial degrees of freedom of the partons. These correlations can be revealed through deeply virtual Compton scattering (DVCS), i.e., the hard exclusive lepto-production of a real photon, which provides access to a three-dimensional (3-D) imaging of partons within the generalized parton distributions (GPDs) framework [22–26]. The measurement of free proton DVCS has been the focus of a worldwide effort [27–35] involving several accelerator facilities such as Jefferson Lab, DESY and CERN. These measurements now enable the extractions of GPDs and a 3-D tomography of the free proton [36, 37]. The aim of this proposal is enhance the neutron GPD measurements along the approved CLAS12 experiment E12-11-003, which will also measure the quasi-free neutron DVCS by detecting the scattered neutron in deuterium.

### 1.2 DVCS Formalism and Observables

The cross section for DVCS on a spin-1/2 target can be parameterized in terms of four helicity conserving GPDs:  $H^q$ ,  $E^q$ ,  $\tilde{H}^q$ , and  $\tilde{E}^q$ . The GPDs  $H$ ,  $E$ ,  $\tilde{H}$  and  $\tilde{E}$  are defined for each quark flavor ( $q = u, d, s, \dots$ ). Analogous GPDs exist for the gluons, see references [?, 23, 26] for details. In this work, we are mostly concerned by the valence quark region,

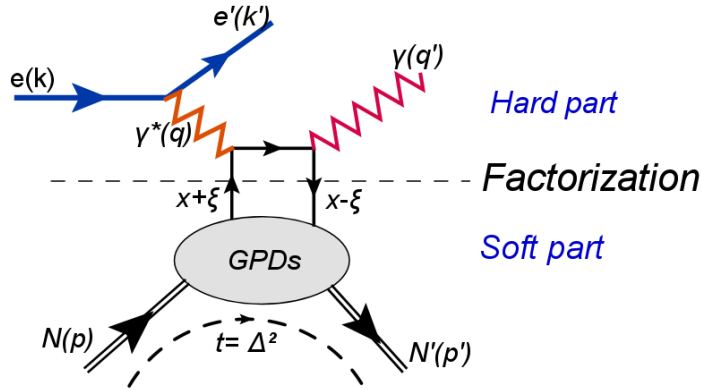


Figure 1.1: Leading-twist DVCS handbag diagram with the momentum definitions labeled.

in which the sea quarks and the gluons contributions do not dominate the DVCS scattering amplitude. The GPDs  $H$  and  $\tilde{H}$  conserve the spin of the nucleon, while  $E$  and  $\tilde{E}$  flip it. The  $H$  and  $E$  GPDs are called the unpolarized GPDs as they represent the sum over the different configurations of the quarks' helicities, whereas  $\tilde{H}$  and  $\tilde{E}$  are called the polarized GPDs because they are made up of the difference between the orientations of the quarks' helicities.

The differential cross section of leptonproduction of photons for a longitudinally-polarized electron beam and an unpolarized nucleon target can be written as:

$$\frac{d\sigma}{dx_B dy dt d\phi d\varphi} = \frac{\alpha^3 x_B y}{16\pi^2 Q^2 \sqrt{1 + \varepsilon^2}} \left| \frac{\mathcal{T}}{e^3} \right|^2 \quad (1.1)$$

where  $\varepsilon \equiv 2x_B \frac{M_n}{Q}$ ,  $x_B = Q^2/(2p_1 \cdot q_1)$  is the Bjorken variable,  $y = (p_1 \cdot q_1)/(p_1 \cdot k_1)$  is the photon energy fraction,  $\phi$  is the angle between the leptonic and hadronic planes,  $\varphi$  is the scattered electron's azimuthal angle,  $Q^2 = -q_1^2$ , and  $q_1 = k_1 - k_2$ . The particle momentum definitions are shown in Figure 1.1. The momentum transfer where the nucleon is initially at rest,  $\Delta = p_1 - p_2$  and  $t = \Delta^2$ . The Bjorken variable is related to the scaling variable by

$$x_B = \frac{Q^2}{2M_N E y} \quad (1.2)$$

where  $M_N$  is the nucleon mass and  $E$  is the beam energy. Another scaling variable called skewedness is

$$\xi = \frac{x_B}{2 - x_B} + \mathcal{O}(1/Q^2) \quad (1.3)$$

The amplitude is the sum of the DVCS, the Bethe-Heitler (BH), and the interference amplitudes, and when squared has terms

$$\mathcal{T}^2 = |\mathcal{T}_{\text{BH}}|^2 + |\mathcal{T}_{\text{DVCS}}|^2 + \mathcal{I} \quad (1.4)$$

where the first is the BH contribution, the second is the DVCS part, and the last term is the interference part,

$$\mathcal{I} = \mathcal{T}_{\text{DVCS}} \mathcal{T}_{\text{BH}}^* + \mathcal{T}_{\text{DVCS}}^* \mathcal{T}_{\text{BH}}. \quad (1.5)$$

The corresponding amplitudes are calculated with the diagrams shown in Figures 1.1 and 1.2. The details of contracting the DVCS tensor with various currents and tensors can be found in [9]. The resulting expressions for the amplitudes are

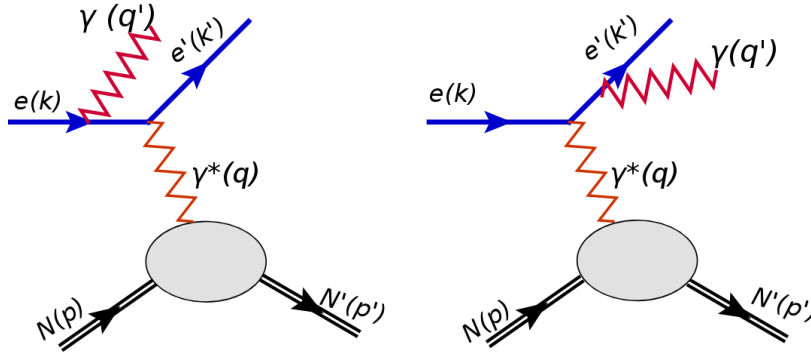


Figure 1.2: BH handbag diagrams.

$$|\mathcal{T}_{\text{BH}}|^2 = \frac{e^6(1+\varepsilon^2)^{-2}}{x_B^2 y^2 t \mathcal{P}_1(\phi) \mathcal{P}_2(\phi)} \left\{ c_0^{\text{BH}} + \sum_{n=1}^2 \left[ c_n^{\text{BH}} \cos(n\phi) + s_n^{\text{BH}} \sin(n\phi) \right] \right\} \quad (1.6)$$

$$|\mathcal{T}_{\text{DVCS}}|^2 = \frac{e^6}{y^2 Q^2} \left\{ c_0^{\text{DVCS}} + \sum_{n=1}^2 \left[ c_n^{\text{DVCS}} \cos(n\phi) + s_n^{\text{DVCS}} \sin(n\phi) \right] \right\} \quad (1.7)$$

$$\mathcal{I} = \frac{e^6(1+\varepsilon^2)^{-2}}{x_B y^3 t \mathcal{P}_1(\phi) \mathcal{P}_2(\phi)} \left\{ c_0^{\mathcal{I}} + \sum_{n=1}^3 \left[ c_n^{\mathcal{I}} \cos(n\phi) + s_n^{\mathcal{I}} \sin(n\phi) \right] \right\} \quad (1.8)$$

The functions  $c_0$ ,  $c_n$ , and  $s_n$  are called *Fourier coefficients* and they depend on the kinematic variables and the operator decomposition of the DVCS tensor for a target with a given spin. At leading twist there is a straightforward form factor decomposition which relates the vector and axial-vector operators with the so-called Compton form factors (CFFs) [?]. The Compton form factors appearing in the DVCS amplitudes are integrals of the type

$$\mathcal{F} = \int_{-1}^1 dx F(\mp x, \xi, t) C^\pm(x, \xi) \quad (1.9)$$

where the coefficient functions at leading order take the form

$$C^\pm(x, \xi) = \frac{1}{x - \xi + i\varepsilon} \pm \frac{1}{x + \xi - i\varepsilon}. \quad (1.10)$$



We plan on measuring the beam spin asymmetry as a function of  $\phi$

$$A_{LU}(\phi) = \frac{d\sigma^{\uparrow}(\phi) - d\sigma^{\downarrow}(\phi)}{d\sigma^{\uparrow}(\phi) + d\sigma^{\downarrow}(\phi)} \quad (1.11)$$

where the arrows indicate the electron beam helicity.

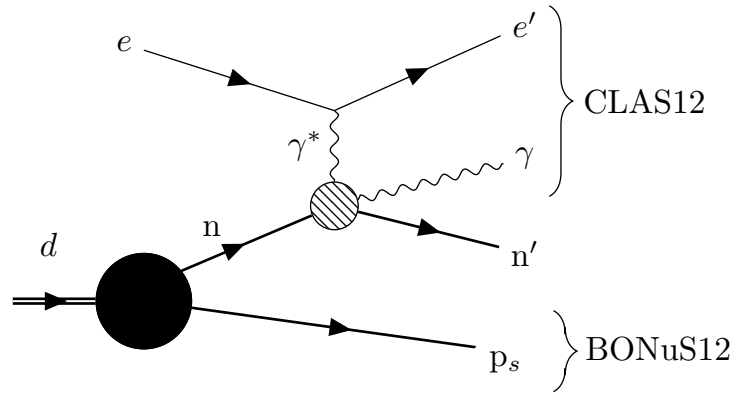


Figure 1.3: Neutron Tagged-DVCS diagram in deuterium.

### 1.3 Tagged neutron DVCS with BONuS12

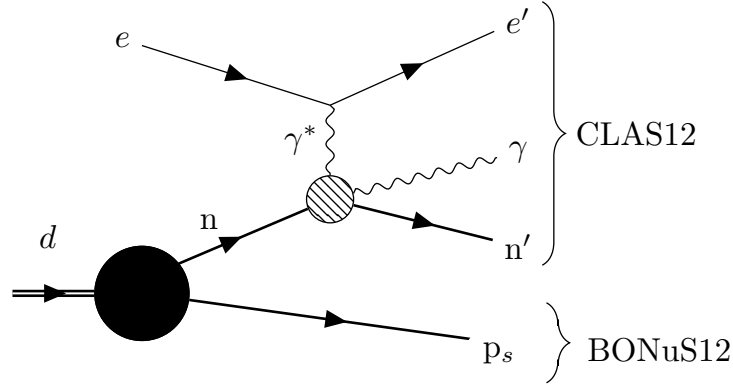
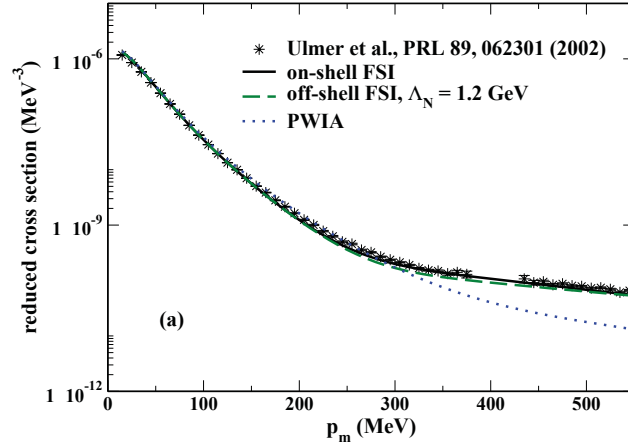


Figure 1.4: Fully exclusive neutron DVCS diagram in deuterium.

Figure 1.5: Reduced quasi-elastic scattering cross section on deuterium. Reproduced from [?]. The reduced cross section includes a term multiplying the cross section by  $M_d f_{\text{rec}} / (\sigma_{\text{Mott}} m_p m_n p_p)$ , where the  $f_{\text{rec}}$  is the recoil factor, and  $\sigma_{\text{Mott}}$  is the Mott cross section.

## 1.4 Fully exclusive neutron DVCS with BONuS12

To understand the regions where FSIs are expected to be significant, we first look at the deuteron. Consider the quasi-elastic scattering on a quasi-free nucleon as shown in Figure 1.4. Measurements of the cross section as a function of missing momentum are shown in Figure 1.5 along with model calculations in PWIA with different final state interactions. From model calculations it was found that the PWIA was insufficient for describing the data at missing momenta above 300 MeV/c. Similarly, the size of the FSI strength as a function of spectator momentum (left) and angle relative to the momentum transfer,  $\theta_s$ , (right) is shown in Figure 1.6 [?, ?]. At low recoil momentum and backwards spectator angle, the FSIs are negligible, where at high momenta perpendicular to the momentum transfer, the FSIs are maximized.

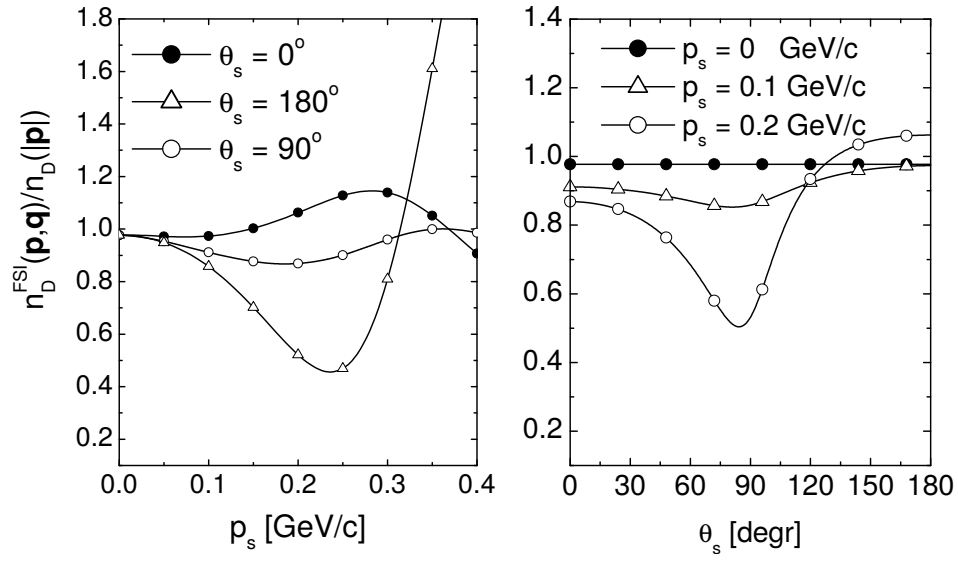


Figure 1.6: Ratio of cross sections for the FSI model from [?] to PWIA calculation as a function of the spectator momentum (left) and spectator angle (right).

# Chapter 2

## Run conditions and Experimental setup

### 2.1 Run Group F conditions

### 2.2 The CLAS12 Spectrometer

The CLAS12 spectrometer is designed to operate with 11 GeV beam at an electron-nucleon luminosity of  $\mathcal{L} = 1 \times 10^{35} \text{ cm}^{-2}\text{s}^{-1}$ . The baseline configuration of the CLAS12 detector consists of the forward detector and the central detector packages [38] (see Figure 2.1). We use the forward detector for electron and photon detection. The central detector's silicon tracker and barrel micromegas will be removed to leave room for the BONuS12 RTPC.

The scattered electrons and photons will be detected in the forward detector which consists of the High Threshold Cherenkov Counters (HTCC), Drift Chambers (DC), the Low Threshold Cherenkov Counters (LTCC), the Time-of-Flight scintillators (TOF), the Forward Calorimeter and the Preshower Calorimeter. The charged particle identification in the forward detector is achieved by utilizing the combination of the HTCC, LTCC and TOF arrays with the tracking information from the Drift Chambers. The HTCC together with the Forward Calorimeter and the Preshower Calorimeter will provide a pion rejection factor of more than 2000 up to a momentum of 4.9 GeV/c, and a rejection factor of 100 above 4.9 GeV/c. The photons are detected using the calorimeters.

### 2.3 BONuS12 RTPC

The new CLAS12 RTPC (BONuS12) is a active 400 mm long cylinder of 160 mm diameter, leaving just enough room to fit adaptive readout boards between the RTPC outer shell and the solenoid. The electric field is directed perpendicularly to the beam direction, such that drifting electrons are pushed away from the beam line. These electrons are amplified by three

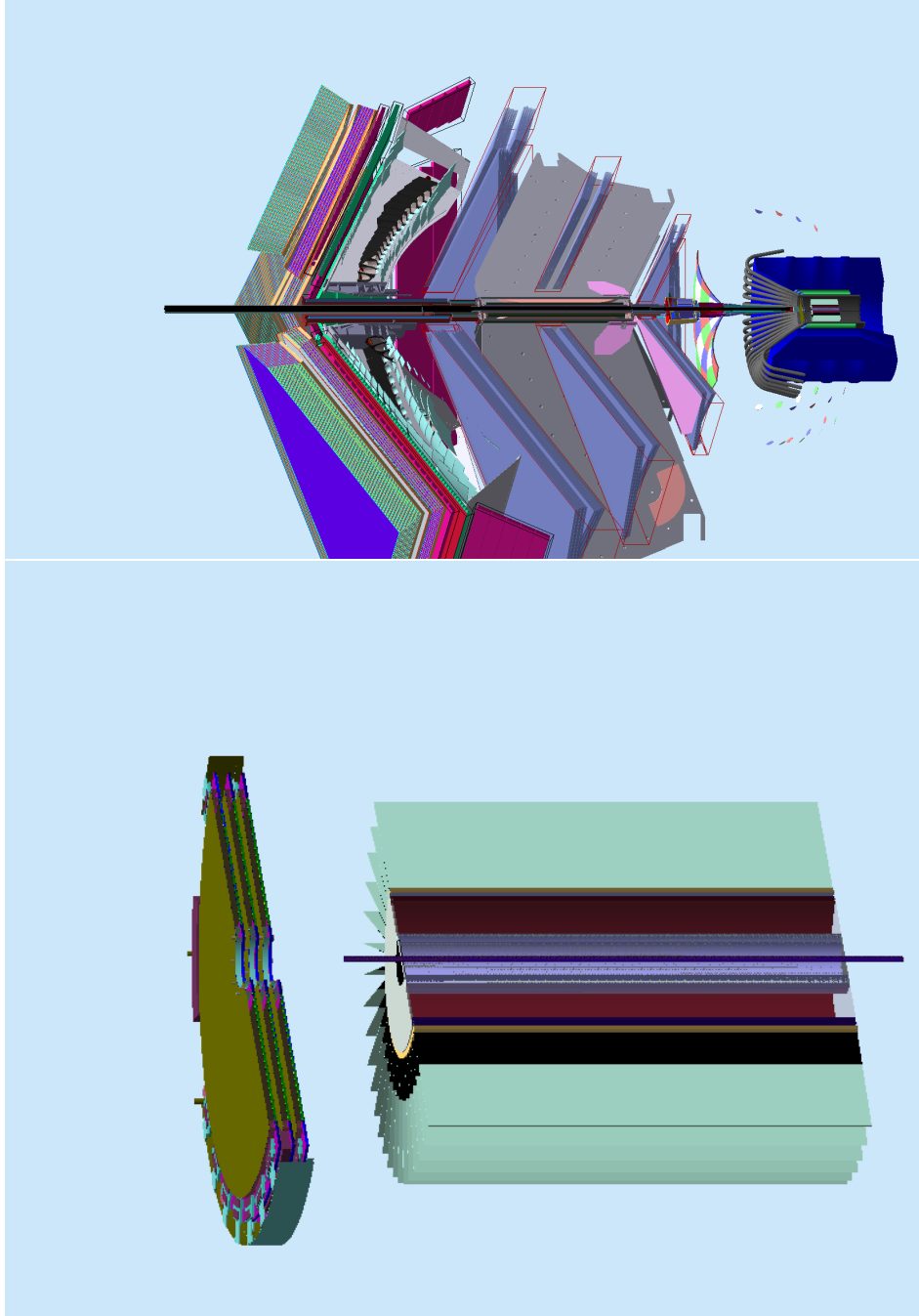


Figure 2.1: (Top) The schematic layout of the CLAS12 baseline design with BONuS12 RTPC replacing the silicon tracker and the barrel micromegas. (Bottom) Schematic layout showing BONuS12 RTPC with the modified design of the forward micromegas.

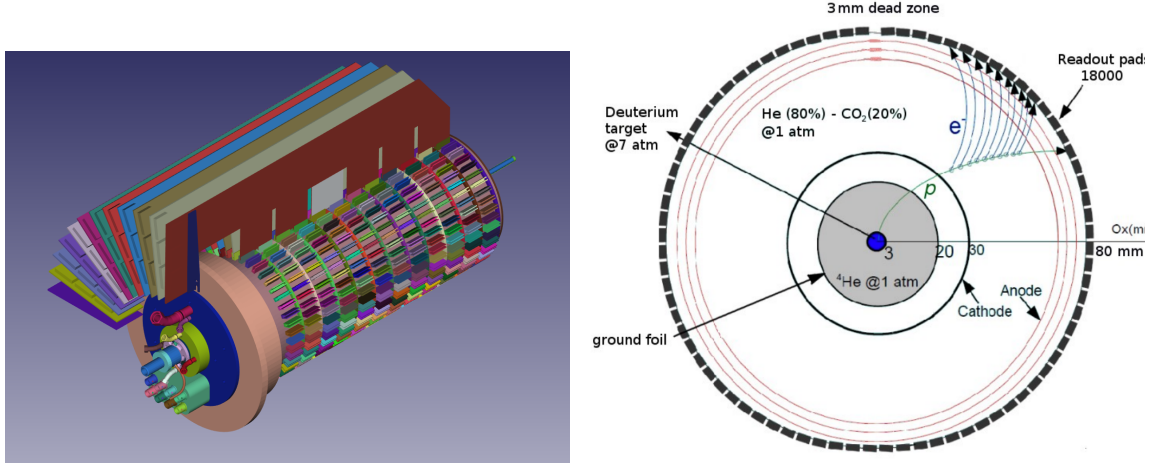


Figure 2.2: (Left) Schematic layout showing BONuS12 RTPC showing the readout padboard and few adaptive boards in addition to the gas lines. (Right) Schematic drawing of the CLAS RTPC in a plane perpendicular to the beam direction. See text for description of the elements.

layers of cylindrical gas electron multipliers (GEM) [?] and detected by the readout system on the external shell of the detector as illustrated in Figure 2.2. The RTPC is segmented into two halves with independent GEM amplification systems that cover almost 100% of the azimuthal angle range.

We detail here the different regions shown in Figure 2.2 starting from the beam line towards larger radius:

- The 7 atm Deuterium gas target extends along the beamline forming the detector central axis. It is a 6 mm diameter Kapton straw with a  $50\ \mu\text{m}$  wall of 492 mm length such that its entrance and exit  $15\ \mu\text{m}$  aluminum windows are placed outside of the detector volume. The detector and the target are placed in the center of the solenoid, 64 cm upstream of the CLAS12 center.
- The first gas gap covers the radial range from 3 mm to 20 mm. It is filled with  $^4\text{He}$  gas at 1 atm to minimize secondary interactions from Møller electrons scattered by the beam. This region is surrounded by a  $4\ \mu\text{m}$  thick window made of grounded aluminized Mylar.
- The second gas gap region extends between 20 mm and 30 mm and is filled with the gas mixture of 80%  $^4\text{He}$  and 20%  $\text{CO}_2$ . This region is surrounded by a  $4\ \mu\text{m}$  thick window made of aluminized Mylar set at  $-4260\ \text{V}$  to serve as the cathode.
- The drift region is filled with the same  $^4\text{He}\text{-CO}_2$  gas mixture and extends from the

cathode to the first GEM, 70 mm away from the beam axis. The electric field in this region is perpendicular to the beam and averages around 550 V/cm.

- The electron amplification system is composed of three GEMs located at radii of 70, 73 and 76 mm. The first GEM layer is set to  $\Delta V = 1620$  V relative to the cathode foil and then each subsequent layer is set to a lower voltage relative to the previous to obtain a strong ( $\sim 1600$  V/cm) electric field between the GEM foils. A 275 V bias is applied across each GEM for amplification.
- The readout board has an internal radius of 79 mm and collects charges after they have been multiplied by the GEMs. Adaptive readout circuit boards are plugged directly on its outer side and transmit the signal to the data acquisition electronics.



# Chapter 3

## Projections for the Proposed Measurements

### 3.1 Monte-Carlo Simulation

An event generator for DVCS/BH and exclusive  $\pi^0$  electroproduction on the neutron inside a deuterium target has been developed [39]. The DVCS amplitude is calculated according to the BKM formalism [40], while the GPDs have been taken from the standard CLAS DVCS generator [41, 42]. The Fermi-motion distribution is calculated with the Paris potential [43].

The output of the event generator was fed through CLAS12 official simulation and reconstruction chain, to simulate the acceptance and resolutions of electrons and photons in the Forward Detector. Final state neutrons being detected in the central detector of CLAS12, and the final state recoiling protons in the BONuS12 RTPC.

Figure 3.1 shows the kinematic distributions of the DVCS electrons being detected and reconstructed in the forward detector of CLAS12 spectrometer in terms of the energy as a function of the polar angle ( $\theta$ ) and the azimuthal angle ( $\phi$ ) as a function of  $\theta$ . Figure 3.4 presents the kinematic distributions of the neutron-DVCS photons detected in the CLAS12 forward detector.

3.4, and ?? show  $\theta$  as a function of momentum in the lab frame and for, respectively, the electron, the photon and the neutron. The two panels of Fig. ?? are one-dimensional plots, showing, respectively, the momentum and the polar angle of the recoil neutron. As expected, the electron and the photon are mostly emitted at forward angles, while the recoil neutron is going at backwards angles.

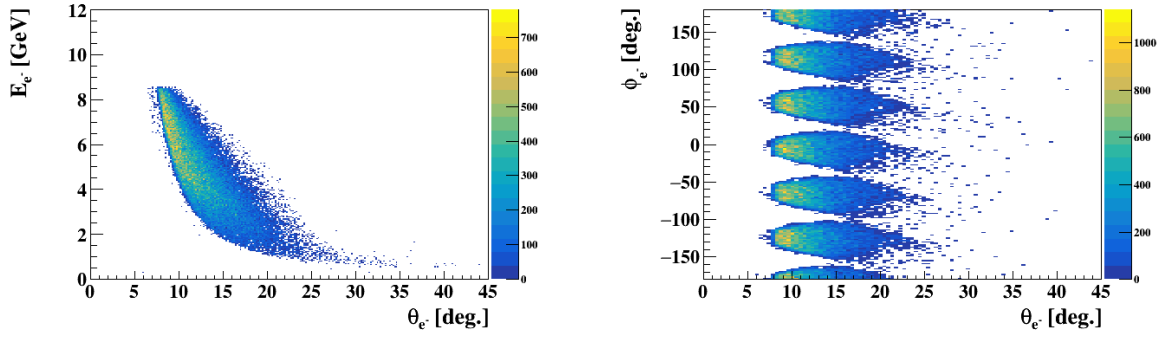


Figure 3.1: Electron's energy as a function of it's polar angle (left) and the azimuthal angle as a function of the polar angle (right), for n-DVCS events. Forward-CLAS12 acceptance and physics cuts are included.

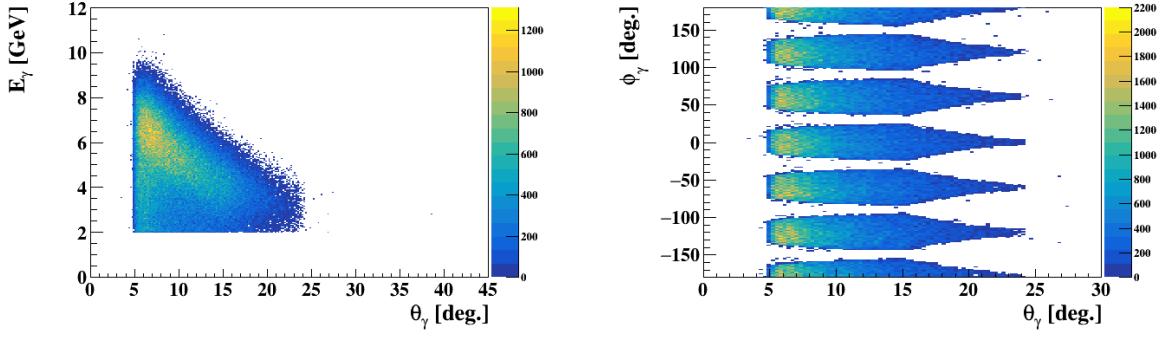


Figure 3.2: Photon's energy as a function of it's polar angle (left) and the azimuthal angle as a function of the polar angle (right), for n-DVCS events. Forward-CLAS12 acceptance and physics cuts are included.

## 3.2 Projections

### 3.2.1 Semi-exclusive selection

### 3.2.2 Semi-exclusive selection

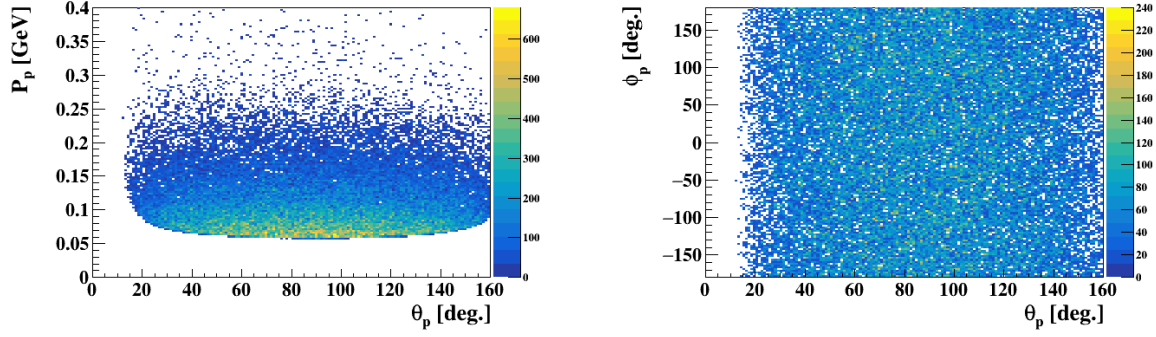


Figure 3.3: Recoiling proton's momentum as a function of its polar angle (left) and the azimuthal angle as a function of the polar angle (right), from n-DVCS events. BONuS12 RTPC acceptance and physics cuts are included.

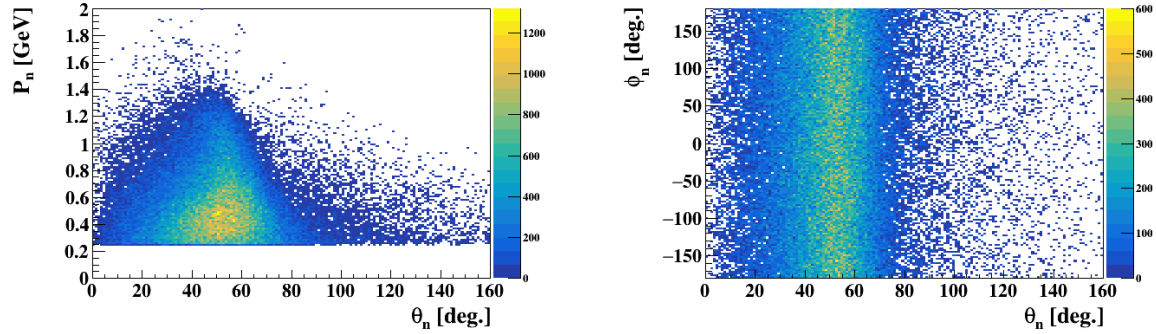


Figure 3.4: Recoiling neutron's momentum as a function of its polar angle (left) and the azimuthal angle as a function of the polar angle (right), from n-DVCS events. BONuS12 RTPC acceptance and physics cuts are included.

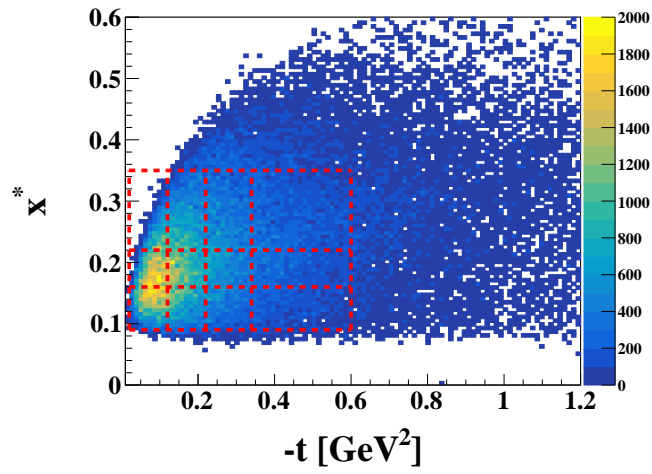


Figure 3.5: Data binning in  $x^*$  vs  $-t$  space.

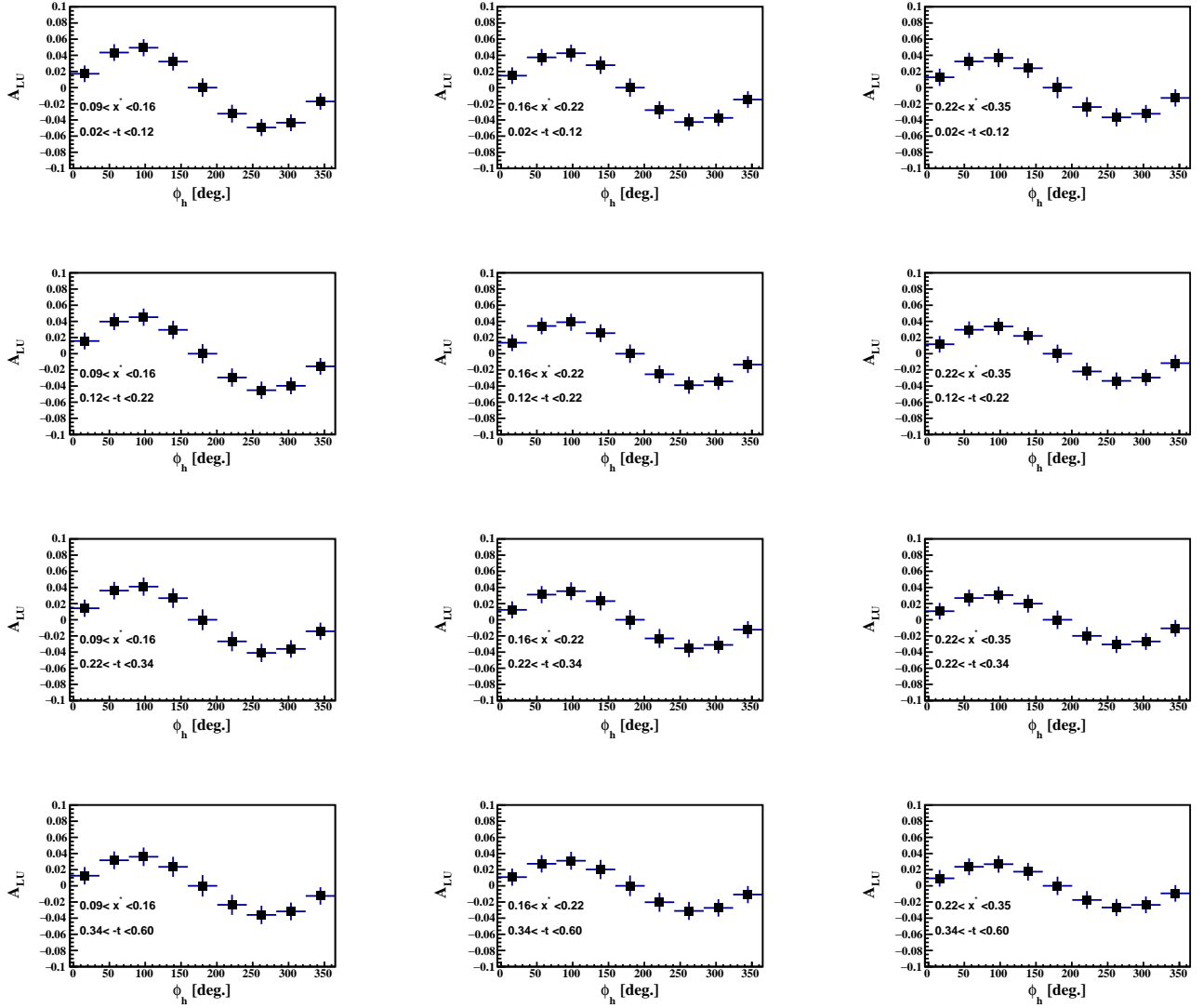


Figure 3.6: Projected beam-spin asymmetries as a function of the hadronic angle  $\phi_h$  in the binning of  $x^*$  vs  $-t$  space.

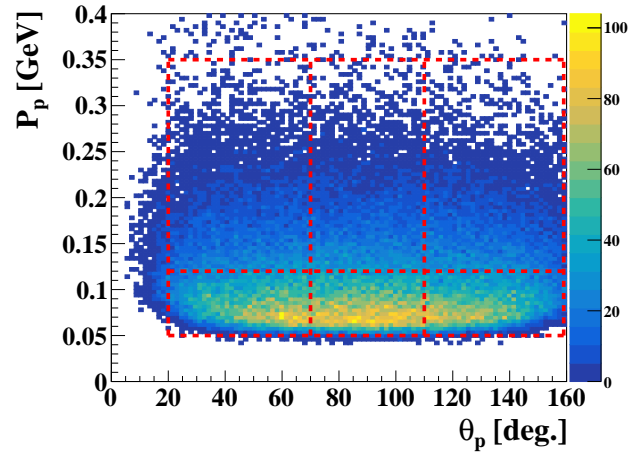


Figure 3.7: Data binning in  $p_s$  vs  $\theta_s$  space.

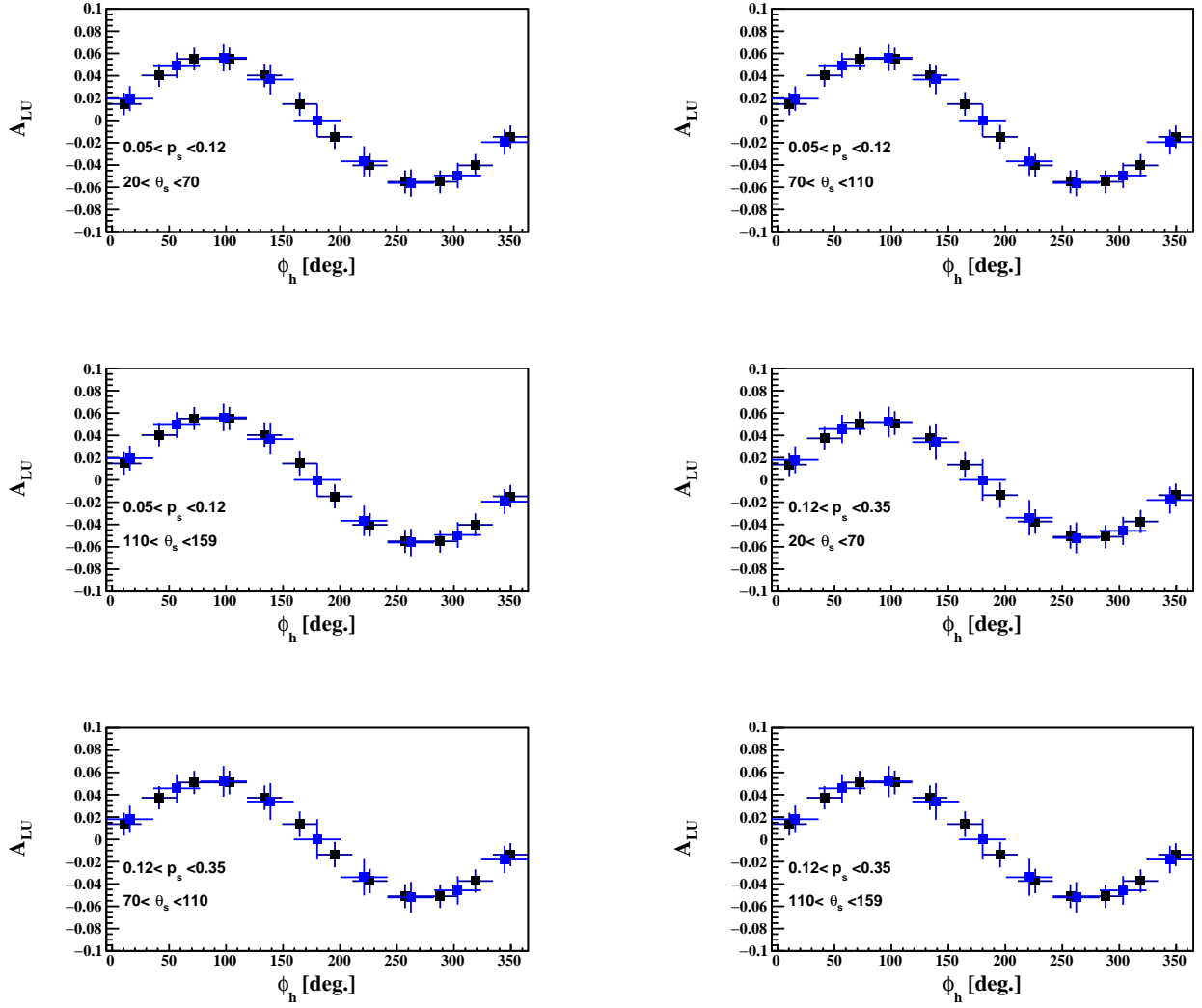


Figure 3.8: Projected beam-spin asymmetries as a function of the hadronic angle  $\phi_h$  in the binning of  $p_s$  vs  $\theta_s$  space.

# Summary



# Bibliography

- [1] J. J. Aubert *et al.*, “The ratio of the nucleon structure functions  $F_2^n$  for iron and deuterium,” *Phys. Lett.*, vol. B123, pp. 275–278, 1983.
- [2] G. A. Miller and J. R. Smith, “Return of the emc effect.,” *Phys.Rev.*, vol. C65, p. 015211, 2002.
- [3] A. W. Thomas, “New insight into nuclear structure from qcd,” *Annalen Phys*, vol. 13, pp. 731–739, 2004.
- [4] S. Liuti and S. K. Taneja, “Nuclear medium modifications of hadrons from generalized parton distributions,” *Phys. Rev.*, vol. C72, p. 034902, 2005.
- [5] A. H. Rezaeian and H.-J. Pirner, “The nuclear matter stability in a non-local chiral quark model,” *Nucl. Phys.*, vol. A769, pp. 35–52, 2006.
- [6] Z.-m. He, X.-x. Yao, C.-g. Duan, G.-l. Li, and H.-g. Peng, “Double  $Q^{*2}$  rescaling model and the nuclear effect of the parton distribution functions,” *Eur. Phys. J.*, vol. C4, pp. 301–306, 1998.
- [7] A. Accardi, D. Grunewald, V. Muccifora, and H. J. Pirner, “Atomic mass dependence of hadron production in deep inelastic scattering on nuclei,” *Nucl. Phys.*, vol. A761, pp. 67–91, 2005.
- [8] A. Accardi, D. Grunewald, V. Muccifora, and H. Pirner, “Erratum: Atomic mass dependence of hadron production in deep inelastic scattering on nuclei,” 2005.
- [9] A. Kirchner and D. Mueller, “Deeply virtual Compton scattering off nuclei,” *Eur. Phys. J.*, vol. C32, pp. 347–375, 2003.
- [10] M. Burkardt, “Impact parameter dependent parton distributions and off-forward parton distributions,” *Phys. Rev.*, vol. D62, p. 071503, 2000.
- [11] M. Diehl, “Generalized parton distributions in impact parameter space,” *Eur.Phys.J.*, vol. C25, pp. 223–232, 2002.
- [12] A. V. Belitsky and D. Mueller, “Nucleon hologram with exclusive leptonproduction,” *Nucl. Phys.*, vol. A711, pp. 118–126,, 2002.

- 
- [13] M. Burkardt, “Transverse deformation of parton distributions and transversity decomposition of angular momentum,” *Phys. Rev.*, vol. D72, p. 094020, 2005.
- [14] R. Hofstadter and R. W. McAllister, “Electron scattering from the proton,” *Phys. Rev.*, vol. 98, pp. 217–218, Apr 1955.
- [15] C. F. Perdrisat, V. Punjabi, and M. Vanderhaeghen, “Nucleon Electromagnetic Form Factors,” *Prog. Part. Nucl. Phys.*, vol. 59, pp. 694–764, 2007.
- [16] M. e. a. Tanabashi, “Review of particle physics,” *Phys. Rev. D*, vol. 98, p. 030001, Aug 2018.
- [17] J. J. Aubert *et al.*, “Measurement of the proton structure function  $F_2$  in muon - hydrogen interactions at 120-GeV and 280-GeV,” *Phys. Lett.*, vol. 105B, pp. 315–321, 1981.
- [18] M. Arneodo, “Nuclear effects in structure functions,” *Physics Reports*, vol. 240, no. 5, pp. 301 – 393, 1994.
- [19] D. F. Geesaman, K. Saito, and A. W. Thomas, “The nuclear EMC effect,” *Ann.Rev.Nucl.Part.Sci.*, vol. 45, pp. 337–390, 1995.
- [20] P. R. Norton, “The EMC effect,” *Rept. Prog. Phys.*, vol. 66, pp. 1253–1297, 2003.
- [21] O. Hen, G. A. Miller, E. Piasetzky, and L. B. Weinstein, “Nucleon-nucleon correlations, short-lived excitations, and the quarks within,” *Rev. Mod. Phys.*, vol. 89, p. 045002, Nov 2017.
- [22] D. M $\tilde{A}$  $\frac{1}{4}$ ller, D. Robaschik, B. Geyer, F. M. Dittes, and J. Horejsi, “Wave functions, evolution equations and evolution kernels from light ray operators of QCD,” *Fortsch. Phys.*, vol. 42, pp. 101–141, 1994.
- [23] X. Ji, “Gauge-invariant decomposition of nucleon spin,” *Phys. Rev. Lett.*, vol. 78, pp. 610–613, Jan 1997.
- [24] X. Ji, “Deeply virtual compton scattering,” *Phys. Rev. D*, vol. 55, pp. 7114–7125, Jun 1997.
- [25] A. V. Radyushkin, “Scaling limit of deeply virtual Compton scattering,” *Phys. Lett.*, vol. B380, pp. 417–425, 1996.
- [26] A. V. Radyushkin, “Nonforward parton distributions,” *Phys. Rev. D*, vol. 56, pp. 5524–5557, Nov 1997.
- [27] S. e. e. Stepanyan, “Observation of exclusive deeply virtual compton scattering in polarized electron beam asymmetry measurements,” *Phys. Rev. Lett.*, vol. 87, p. 182002, Oct 2001.

- 
- [28] A. e. e. Airapetian, “Measurement of the beam-spin azimuthal asymmetry associated with deeply-virtual compton scattering,” *Phys. Rev. Lett.*, vol. 87, p. 182001, Oct 2001.
- [29] A. e. e. Airapetian, “Beam-charge azimuthal asymmetry and deeply virtual compton scattering,” *Phys. Rev. D*, vol. 75, p. 011103, Jan 2007.
- [30] F. X. Girod *et al.*, “Measurement of Deeply virtual Compton scattering beam-spin asymmetries,” *Phys. Rev. Lett.*, vol. 100, p. 162002, 2008.
- [31] M. e. e. Defurne, “E00-110 experiment at jefferson lab hall a: Deeply virtual compton scattering off the proton at 6 gev,” *Phys. Rev. C*, vol. 92, p. 055202, Nov 2015.
- [32] M. e. e. Mazouz, “Deeply virtual compton scattering off the neutron,” *Phys. Rev. Lett.*, vol. 99, p. 242501, Dec 2007.
- [33] G. e. e. Gavalian, “Beam spin asymmetries in deeply virtual compton scattering (dvcs) with clas at 4.8 gev,” *Phys. Rev. C*, vol. 80, p. 035206, Sep 2009.
- [34] E. e. e. Seder, “Longitudinal target-spin asymmetries for deeply virtual compton scattering,” *Phys. Rev. Lett.*, vol. 114, p. 032001, Jan 2015.
- [35] H. S. Jo *et al.*, “Cross sections for the exclusive photon electroproduction on the proton and Generalized Parton Distributions,” *Phys. Rev. Lett.*, vol. 115, no. 21, p. 212003, 2015.
- [36] M. Guidal, H. Moutarde, and M. Vanderhaeghen, “Generalized Parton Distributions in the valence region from Deeply Virtual Compton Scattering,” *Rept. Prog. Phys.*, vol. 76, p. 066202, 2013.
- [37] R. Dupré, M. Guidal, and M. Vanderhaeghen, “Tomographic image of the proton,” *Phys. Rev. D*, vol. 95, p. 011501, Jan 2017.
- [38] “CLAS12 Technical Design Report,” 2008.
- [39] A. E. Alaoui and E. Voutier *CLAS Note 2009-024*.
- [40] A. V. Belitsky, D. Mueller, and A. Kirchner, “Theory of deeply virtual Compton scattering on the nucleon,” *Nucl. Phys.*, vol. B629, pp. 323–392, 2002.
- [41] M. Vanderhaeghen, P. A. M. Guichon, and M. Guidal, “Deeply virtual electroproduction of photons and mesons on the nucleon: Leading order amplitudes and power corrections,” *Phys. Rev. D*, vol. 60, p. 094017, Oct 1999.
- [42] M. Guidal, M. V. Polyakov, A. V. Radyushkin, and M. Vanderhaeghen, “Nucleon form-factors from generalized parton distributions,” *Phys. Rev.*, vol. D72, p. 054013, 2005.

- 
- [43] M. Lacombe, B. Loiseau, J. M. Richard, R. V. Mau, J. Côté, P. Pirès, and R. de Tournell, “Parametrization of the paris  $n - n$  potential,” *Phys. Rev. C*, vol. 21, pp. 861–873, Mar 1980.